# Rapid hydrothermal flow synthesis and characterisation of carbonate- and silicate-substituted calcium phosphates

**Aqif A Chaudhry[1,2], Jonathan C Knowles[3,4], Ihtesham Rehman[5] and Jawwad A Darr[1]**

## Abstract

A range of crystalline and nano-sized carbonate- and silicate-substituted hydroxyapatite has been successfully produced by using continuous hydrothermal flow synthesis technology. Ion-substituted calcium phosphates are better candidates for bone replacement applications (due to improved bioactivity) as compared to phase-pure hydroxyapatite. Urea was used as a carbonate source for synthesising phase pure carbonated hydroxyapatite ($CO_3$-HA) with $\approx 5$ wt% substituted carbonate content (sample $7.5CO_3$-HA) and it was found that a further increase in urea concentration in solution resulted in biphasic mixtures of carbonate-substituted hydroxyapatite and calcium carbonate. Transmission electron microscopy images revealed that the particle size of hydroxyapatite decreased with increasing urea concentration. Energy-dispersive X-ray spectroscopy result revealed a calcium deficient apatite with Ca:P molar ratio of 1.45 ($\pm 0.04$) in sample $7.5CO_3$-HA. For silicate-substituted hydroxyapatite ($SiO_4$-HA) silicon acetate was used as a silicate ion source. It was observed that a substitution threshold of $\sim 1.1$ wt% exists for synthesis of $SiO_4$-HA in the continuous hydrothermal flow synthesis system, which could be due to the decreasing yields with progressive increase in silicon acetate concentration. All the as-precipitated powders (without any additional heat treatments) were analysed using techniques including Transmission electron microscopy, X-ray powder diffraction, Differential scanning calorimetry, Thermogravimetric analysis, Raman spectroscopy and Fourier transform infrared spectroscopy.

## Keywords

Calcium phosphates, bioactive, silicate, carbonate, substituted

## Introduction

Synthetic hydroxyapatite (HA, $Ca_{10}(PO_4)_6(OH)_2$, Ca:P molar ratio 1.67), is a bioactive material that is chemically similar to biological apatite, the mineral component of bone.[1] However, biological apatite is a poorly crystalline, non-stoichiometric material (Ca:P molar ratio $< 1.67$) that contains additional ions in the structure ($Na^+, SiO_4^{4-}, CO_3^{2-}, Zn^{2+}, Mg^{2+}$ etc.).[2–6] HA is used widely as a bone graft substitute,[7] reinforcement in composites,[8–11] porous scaffold[12] and bioactive coatings,[13,14] etc.

Human bone contains up to 8 wt% carbonate ions that occupy phosphate and hydroxide positions in the apatite lattice.[15] It has been shown that the presence of carbonate in synthetic HA leads to structural disorder and a higher solubility.[15,16] This is useful because although HA can bond to surrounding tissue, this process is very slow.[17] Carbonate-substituted HA is therefore, considered as an optimised biomaterial, which

leads to faster bonding between an inserted implant surface and human bone.[17–21]

Substitution of carbonate ions in the HA lattice can be of two types, A-type, where carbonate ion substitutes the hydroxyl ion and B-type, where the carbonate

[1]Clean Materials Technology Group, Department of Chemistry, University College London, Christopher Ingold Laboratories, London, UK
[2]Interdisciplinary Research Centre in Biomedical Materials (IRCBM), COMSATS Institute of Information Technology, M. A. Jinnah Campus, Lahore, Pakistan
[3]Division of Biomaterials and Tissue Engineering, UCL Eastman Dental Institute, London, UK
[4]WCU Research Centre of Nanobiomedical Science, Dankook University, Dongnam-gu, Cheonan-si, Chungnam, South Korea
[5]The Kroto Research Institute, North Campus, University of Sheffield, Broad Lane, Sheffield, UK

**Corresponding author:**
Aqif A Chaudhry, Interdisciplinary Research Centre in Biomedical Materials (IRCBM), COMSATS Institute of Information Technology, M. A. Jinnah Campus, Lahore, Pakistan.
Email: aqifanwar@ciitlahore.edu.pk

ion substitutes the phosphate ion.[15,16,22,23] A-type carbonated HA can be formed when carbon dioxide gas is passed over HA at high temperature in the range 500–1100°C.[15,16] This substitution reaction can be represented as follows

$$Ca_{10}(PO_4)_6(OH)_2 + xCO_2 \rightarrow$$
$$Ca_{10}(PO_4)_6(OH)_{2-2x}(CO_3)_x + xH_2O \quad (1)$$
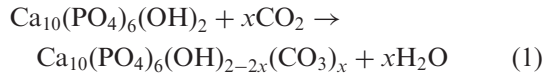
B-type CHA can be formed by precipitation from solution and can give a material with less particle crystallinity and smaller crystal size.[15,16] B-type carbonate substitution is more complicated than A-type carbonate substitution into HA. Carbonate ions ($CO_3^{2-}$) substituting for phosphate ions ($PO_4^{3-}$) require a reduction in the number of calcium ions to maintain charge balance. Kühl and Nebergall[24] in 1963 proposed the following formula for B-type carbonate-substituted HA

$$Ca_{10-x+y}(CO_3)_x(PO_4)_{6-x}(OH)_{2-x+2y} \quad (2)$$
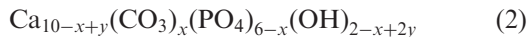
Sodium ions ($Na^+$) can partially substitute calcium ions ($Ca^{2+}$) in HA leading to stabilisation of a B-type carbonate-substituted HA.[23,25] This substitution leads to $Ca_{10-x}Na_x(PO_4)_{6-x}(CO_3)_x(OH)_2$. The charge balance can be represented as follows

$$Na^+ + CO_3^{2-} \leftrightarrow Ca^{2+} + PO_4^{3-} \quad (3)$$
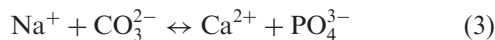
In reports by Vignoles et al.[26] and Doie et al.[27] ammonium carbonate was used as a carbonate source, in order to avoid using a sodium-based source. However, this resulted in incorporation of ammonium ions ($NH_4^+$) in the HA lattice. Absorption bands corresponding to the ammonium ion ($NH_4^+$) have been reported to appear at 3200 and 1400 $cm^{-1}$ in FTIR spectra.[28] Gibson et al.[23] later reported synthesis of carbonate-substituted HA using carbonated water, which avoided incorporation of unwanted ions in the HA lattice. Carbonate-substituted HA has also been synthesised at 140°C in 24 h under autogenous pressure using a batch hydrothermal process with urea as a carbonate source.[29] Hydrothermal treatment has also been used to form carbonate-substituted HA coatings using plasma spray-coated brushite as a precursor material.[30]

In addition to calcium phosphates, calcium carbonate is also a known biocompatible material.[31–33] Indeed, calcium carbonate implants have been studied, due to their relatively faster resorption, and therefore, quicker onset of neo bone formation. Three weeks after implantation 10.8% bone formation was observed under microscope as compared to 4.8% for HA implants inserted in muscular cavities of rats.[32,34]

Bone regeneration, around dental implants used in alveolar ridge treatment, has been reported after use of compositions which included calcium carbonate.[35] Stephen Mann's research group based at University of Bristol has reported extensively on morphological and phase control of calcium carbonate particles synthesised using microemulsions and its biological uses.[36,37] However, complete resorption of a porous bone substitute (before bone has filled the pores), is disadvantageous as a controlled replacement is preferred.[32] Hence, calcium carbonate and calcium phosphate mixtures are of interest as they may offer tailorable dissolution and regrowth rates. This way the defect is able to function or take a load whilst the repair process is underway.

Although HA is known to be bioactive and osteoconductive, it has a relatively slow rate of dissolution and osseointegration.[38] One of the methods to improve the osseointegration of HA is to substitute traces of elements such as silicon, in the HA lattice.[39] One of the earliest works on role of silicon in bone was reported in the 1970s by Carlisle, wherein the presence of 0.5 wt% silicon was reported in mineralising osteoid regions in young mice and rats.[40] Silicon has also been reported to play an important role in the formation of collagen.[41] Silicon-substituted HA (Si-HA) has been reported to promote rapid bone mineralisation; however, it also leads to a smaller crystallite size and faster dissolution.[42–45] Use of silicon-substituted HA as sintered granules in femoral condyles of rabbits resulted in significantly greater bone formation (37.5%) when compared (after 23 days of implantation) with the case where phase-pure HA (22.0%) was used.[45] Due to the importance attached to presence of silicon in calcifying regions of bone, attempts have been made to incorporate silicon in the HA lattice. Silicon-substituted HA has been synthesised using wet-precipitation and batch hydrothermal techniques.[46–50] There have also been many reports on the development of silicon-substituted HA coatings on metallic substrates for enhanced osseointegration.[14,51,52] Silicon enters the HA lattice in the form of silicate ions ($SiO_4^{4-}$), which substitute for phosphate ions ($PO_4^{3-}$). Silicon levels of up to 4 wt% in HA have been reported using a batch hydrothermal process.[49,53] This substitution can be represented as follows

$$Ca_{10}(PO_4)_6(OH)_2 + xSiO_4^{4-} \rightarrow Ca_{10}(PO_4)_{6-x}$$
$$(SiO_4)_x(OH)_{2-x} + xPO_4^{3-} + xOH^{-1} \quad (4)$$
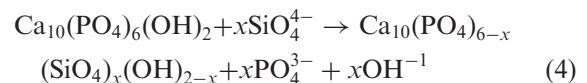
The current methods for the synthesis of nano-sized calcium phosphates (and ion-substituted calcium phosphates) can be slow, irreproducible or involve use of organic solvents.[54,55] Supercritical fluids such as

supercritical water (critical temperature $T_c = 374°C$; critical pressure, $P_c = 22.1$ MPa) and carbon dioxide have attracted interest for a range of materials processes due to their exotic reaction conditions, lack of solvent residues and often enhanced diffusion or reaction kinetics.[56–59] A supercritical fluid is a single phase fluid in which the substance is neither a fluid or a gas but can possess the properties of both simultaneously. Continuous hydrothermal flow synthesis of nanoparticles (using a flow of supercritical water) is a route that allows rapid, single step synthesis of ceramic nanoparticles for diverse applications.[60–67] The authors previously demonstrated in an initial communication that the rapid crystallising continuous environment in a CHFS system, resulted in one-step rapid formation of HA.[68] In a further publication, the authors reported the use of CHFS for the rapid and direct manufacture of magnesium containing calcium phosphates.[69] The authors have also highlighted the benefits of the CHFS technology to obtain nano-sized HA (and ceramic–ceramic nanomixtures) which sinters to translucent fully dense discs under spark plasma sintering whilst retaining its nanostructure and high flexural strength.[70,71]

Herein CHFS was used to incorporate carbonate and silicate ions into the HA lattice. These materials were characterised using various analytical techniques to assess the effects of silicate and carbonate substitution.

## Experimental section

### Materials and equipment

Diammonium hydrogen phosphate, [$(NH_4)_2HPO_4$, 98.3%], calcium nitrate tetrahydrate [$Ca(NO_3)_2.4H_2O$, 99%] and silicon tetraacetate [$Si(OCOCH_3)_4$, 98%] were supplied by Sigma-Aldrich Chemical Company (Dorset, UK) and used as obtained. Ammonium hydroxide solution ($NH_4OH$, ≥30% w/w) used to adjust the solutions' pH, and Urea [$(NH_2)_2CO$, 99.5%] were supplied by VWR International (UK). Ten mega-ohms deionised water was used in all reactions.

Samples were freeze-dried using a Vitris Advantage Freeze Dryer, Model 2.0 ES, supplied by BioPharma. A JEOL 2010 transmission electron microscope (TEM) (200 kV accelerating voltage) was used for generating images of particles. An Oxford Instruments Inca 400 EDX (energy-dispersive X-ray spectroscopy) detector connected to a scanning electron microscope (JEOL 5410 LZSEM) was used to carry out elemental analysis for all the samples. Averages of 10 area scans were used to calculate average elemental composition. The SEM was operated at 25 kV and all samples were carbon coated prior to measurement. Image Tool UTHSCSA version 3.0 software was used for estimating particle size.

PXRD (Powder X-ray Diffraction) data were collected on a Siemens D5000 X-Ray diffractometer using Cu-K$\alpha$ radiation ($\lambda = 1.5418$ Å) over the $2\theta$ range 5–70° with a step size of 0.02° and a count time of 1 s.

Simultaneous differential scanning calorimetry (DSC) and thermogravimetric analyses (TGA) were carried out using a Polymer Labs STA 1500 using a heating rate of 10°C/min in the 30–1200°C temperature range under nitrogen. A Nicolet Almega dispersive Raman spectrometer (785 nm laser) was used in the wavenumber range 1200–400 cm$^{-1}$ averaging 20 scans for 2 s each. Fourier transform infrared (FTIR) spectra of the samples were collected using a Nicolet FTIR 800 spectrometer fitted with a photoacoustic sampler (MTech PAS Cell). Spectra were obtained in the range 4000–400 cm$^{-1}$, at 8 cm$^{-1}$ resolution averaging 256 scans. BET surface area measurements (using $N_2$ gas adsorption method), were performed on a Micromeritics Gemini analyser; powders were first degassed at 80°C for 3 h prior to analyses. 29Si magic angle spinning nuclear magnetic resonance (MAS-NMR) was carried for sample 5-SiHA using the solid-state NMR research service at Department of Chemistry, Durham University.

### Synthesis and methodology

*Carbonate ($CO_3^{2-}$)-substituted calcium phosphate.* In total, five separate reactions were carried out for this study. Urea (carbonate ion source) was added to diammonium hydrogen phosphate to result in overall 50.0 mM concentration (adjusted pH 10). This solution was reacted with 83.5 mM calcium nitrate solution (adjusted pH 11). The pH of both the solutions was adjusted using neat ammonium hydroxide solution. It was assumed that carbonate enters the HA lattice according to; [$Ca_{10}(PO_4)_{6-y}(CO_3)_y(OH)_2$], where in it was assumed that B-type carbonate substitution takes place. Samples are labelled as 7.5$CO_3$-HA, 11.5$CO_3$-HA, 15.7$CO_3$-HA, 20$CO_3$-HA and 24.6$CO_3$-HA. The numbers in the sample IDs represent the nominal (expected) carbonate content (wt%). Other details on the preparation of solutions are shown in Table 1.

A continuous hydrothermal flow synthesis (CHFS) system with three HPLC pumps and similar to that described elsewhere, was used for syntheses (Figure 1).[64,72–74] Briefly, the CHFS system allows pumping and then mixing of the Ca salt and a basic phosphate source (with urea) at a ¼" stainless steel Swagelok$^{TM}$ T-piece mixer (whereupon initial precipitation at ambient temperature occurs in flow).

**Table 1.** Sample IDs, expected wt% of carbonate, *y* values (according to $Ca_{10}(PO_4)_{6-y}(CO_3)_y(OH)_2$) and corresponding amounts of reagents used.

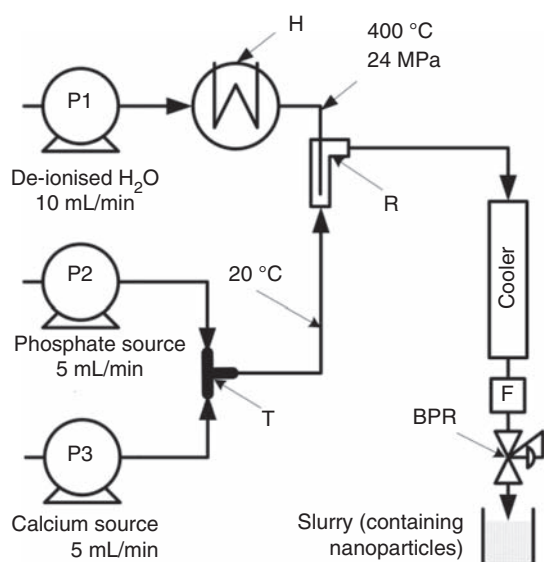| Sample ID | Carbonate wt% | *y* | $(NH_4)_2HPO_4$ (300 mL deionised water) | |
|---|---|---|---|---|
| | | | mmoles | wt (g) |
| 7.5CO₃-HA | 7.5 | 1.2 | 12.0 | 1.59 |
| 11.5CO₃-HA | 11.5 | 1.8 | 10.5 | 1.39 |
| 15.7CO₃-HA | 15.7 | 2.4 | 9.0 | 1.19 |
| 20CO₃-HA | 20.0 | 3.0 | 7.5 | 0.99 |
| 24.6CO₃-HA | 24.6 | 3.6 | 6.0 | 0.79 |



**Figure 1.** Scheme of the three-pump continuous hydrothermal flow synthesis system used for the preparation of Mg-substituted calcium phosphates. Key: P = HPLC pump, H = heater, C = cooler, F = filter, B = back-pressure regulator, R = counter-current reactor, T = stainless steel T-piece mixer.

This slurry then meets the flow of superheated water in a stainless steel counter-current mixer,[68,72] whereupon the bioceramic material is crystallised in a continuous fashion. The products are then cooled, filtered to remove large agglomerates and pass out of a back-pressure regulator which maintains system pressure. Pump rates of 10.0, 5.0 and 5.0 mL/min were used for the superheated water feed, calcium nitrate and diammonium hydrogen phosphate/urea solutions, respectively. A Ca:$[PO_4^{3-} + CO_3^{2-}]$ molar ratio of ~1.67 was hence maintained in all reagent solutions. All reactions were carried out using a superheated water feed at 400°C and 24 MPa. All samples were centrifuged, washed and freeze-dried.

*Silicate ($SiO_4^{2-}$)-substituted calcium phosphate.* In total, eight reactions were carried out for this section of the study. Silicon acetate was used as a silicate ion source and was dissolved in 83.5 mM calcium nitrate (pH 3.5). The diammonium hydrogen phosphate solutions were prepared such that the combined concentration of silicate and phosphate ions was 50 mM. The pH of diammonium hydrogen phosphate solution was adjusted to pH 10 using neat ammonium hydroxide solution. The pH of the calcium nitrate solution (which contained dissolved silicon acetate) was not adjusted as it was observed that it reacted with ammonium hydroxide to result in a murky suspension. It was assumed that silicate replaces phosphate in the HA lattice according to $[Ca_{10}(PO_4)_{6-x}(SiO_4)_x(OH)_{2-x}]$. Samples are labelled as 1SiHA, 2SiHA, 3SiHA, 4SiHA, 5SiHA, 6SiHA, 8SiHA and 10SiHA. The numbers in the samples IDs represent the theoretically expected amount of silicon content (wt%). Other details on the preparation of solutions are shown in Table 2.

A similar CHFS system (as used for carbonate substitution, Figure 1) was used for these reactions and pump rates of 10.0, 5.0 and 5.0 mL/min were used for superheated water feed, combined calcium nitrate/silicon acetate feed and diammonium hydrogen phosphate solutions, respectively. A Ca:$[PO_4^{3-} + SiO_4^{4-}]$ molar ratio of ~1.67 was hence maintained in all reactions. All reactions were carried out using a superheated water feed at 400°C and 24 MPa.

## Results and discussion

TEM was carried out to determine particle size and morphology. Figure 2(a) for sample 7.5CO₃-HA shows rods of size ~146 (±77) × 50 (±18) nm (aspect ratio ~2.92, 50 particles sampled). Deviation from strict rod-like shape of particles of HA as reported in the previous study, was evident.[68] The particle size was further reduced with increasing carbonate content, from ~109 (±34) × 41 (±10) nm in Figure 2(b) for sample 15.7CO₃-HA (aspect ratio ~2.7, 50 particles sampled) to ~64 (±34) × 27 (±8) nm in Figure 2(c) for sample 24.6CO₃-HA (aspect ratio ~2.4, 50 particles sampled). The cube-like morphology of some particles in Figure 2(c) was similar to that of calcium carbonate (calcite) as reported in a previous TEM investigation.[75]

TEM was also carried out to assess the effect of silicon substitution in HA on particle morphology and size. Figure 3(a) and (b) shows TEM images of HA (synthesis reported earlier[68]) [~140 (±58) × 40 (±12), aspect ratio 3.5] and sample 5SiHA (~184 (±28) × 41 (±7) nm, aspect ratio 4.4, 50 particles sampled), respectively. It was observed that the presence of silicon slightly increased the particle size (aspect ratio changes

**Table 2.** Sample IDs, expected wt% of silicon, *x* values (according to $Ca_{10}(PO_4)_{6-x}(SiO_4)_x(OH)_{2-x}$) and corresponding amounts of reagents used.

| | | | $(NH_4)_2HPO_4$ (in 100 mL deionised water) | | $Si(OCOCH_3)_4$ (added to 100 mL $(NH_4)_2HPO_4$ solution) | |
|---|---|---|---|---|---|---|
| Sample ID | Silicon Wt% | x | mmoles | Wt (g) | mmoles | Wt (g) |
| 1SiHA | 1 | 0.4 | 4.7 | 0.62 | 0.3 | 0.08 |
| 2SiHA | 2 | 0.7 | 4.4 | 0.58 | 0.6 | 0.15 |
| 3SiHA | 3 | 1.0 | 4.1 | 0.55 | 0.9 | 0.23 |
| 4SiHA | 4 | 1.4 | 3.9 | 0.51 | 1.1 | 0.30 |
| 5SiHA | 5 | 1.7 | 3.6 | 0.47 | 1.4 | 0.37 |
| 6SiHA[a] | 6 | 2.0 | 1.7 | 0.22 | 0.8 | 0.22 |
| 8SiHA[a] | 8 | 2.6 | 1.4 | 0.19 | 1.1 | 0.29 |
| 10SiHA[a] | 10 | 3.2 | 1.2 | 0.16 | 1.3 | 0.35 |

[a]These reactions were run at half concentration due to the inability to dissolve silicon acetate in 83.5 mM calcium nitrate solution.
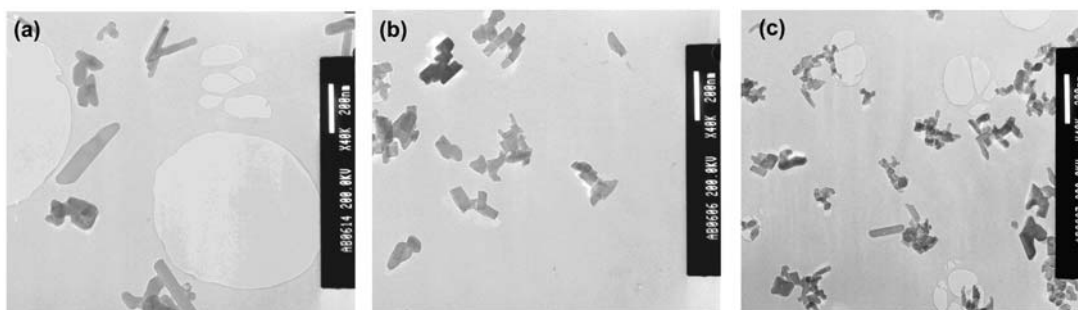


**Figure 2.** Transmission electron microscope images of: (a) sample 7.5CO$_3$-HA at ×40 k magnification (bar = 200 nm); (b) sample 15.7CO$_3$-HA at ×40 k magnification (bar = 200 nm) and (c) sample 24.6CO$_3$-HA at ×40 k magnification (bar = 200 nm).
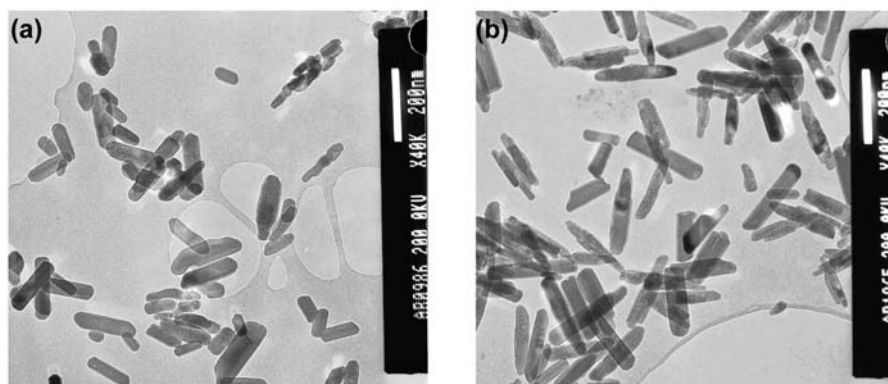


**Figure 3.** Transmission electron microscope images of: (a) HA at ×40 k magnification (bar = 200 nm) and (b) 5SiHA at ×40 k magnification (bar = 200 nm).

from ~3.5 to 4.4), narrows the size distribution (lower standard deviations) as compared to HA and makes the nanorods less defined on its growing edges. The TEM investigation suggested opposite effects of presence of carbonate ions as compared to that of silicate ions in solution on particle size and morphology.

The Ca:P molar ratio of sample 7.5CO$_3$-HA was determined to be ~1.45 (±0.04) using an EDX detector attached to a SEM (each area is averaged from 5 measurements). The elemental compositions for carbonate-substituted samples are reported in Supplementary Data Table 1 (later found out to be biphasic mixtures).

Carbonate contents were determined using simultaneous TGA and DSC. The corresponding plots for samples 7.5CO$_3$-HA and 24.6CO$_3$-HA are shown in Figure 4. TGA and DSC plots for remaining carbonate-substituted samples are reported in Supplementary Data Figure 1. The TGA and DSC plots for sample 7.5CO$_3$-HA shown in Figure 4(a) showed three overlapping regions of weight loss at 30–200°C (2.2 wt%), 200–460°C (1.7 wt%) and 460–990°C (3.7 wt%). Thereafter there was a sudden weight loss (8.2 wt%) up to 1200°C to give a final weight loss of 15.8 wt%. The first weight loss was presumably due to loss of weakly associated water, whilst the loss of lattice water and CO$_2$ occur for the second and third weight losses respectively. Decomposition accounted for the weight loss after 990°C.

The carbonate content was calculated to be around ca. 5 wt%. DSC plot for sample 7.5CO$_3$-HA in Figure 4(a) revealed a broad endotherm corresponding to loss of weakly associated water at ~70°C. An endotherm centred at ~700°C corresponded to the weight loss due to loss of CO$_2$ from sample 7.5CO$_3$-HA. Figure 4(b) shows TGA and DSC plots for sample 24.6CO$_3$-HA, which were similar to those for sample 7.5CO$_3$-HA (Figure 4(a)). However, the weight loss in the range 470°C and 983°C was 18 wt% (loss of CO$_2$). The carbonate content was calculated to be around 24.5 wt%. This CO$_2$ loss corresponds to carbonate loss from the apatite lattice and CaCO$_3$ (as determined using XRD, explained in the following sections). The expected carbonate contents in HA and measured carbonate contents are summarised in Table 3.

EDX was used to determine the elemental compositions of silicate-substituted samples as shown in Table 4. It was noticed that the obtained silicon contents (Table 4) were markedly less compared to expected content unlike for carbonate substitution.

Moreover, the percentage theoretical yield decreased with increasing silicon content in the solution. This suggested that there was a threshold for silicon substitution into HA using CHFS technique (using current parameters) with silicon acetate as a silicate ion source.

**Table 3.** Expected and measured carbonate content (determined using TGA) of carbonate substituted samples.

| Sample ID | Expected carbonate content in HA (wt%) | Measured carbonate content in sample |
|---|---|---|
| 7.5CO$_3$-HA | 7.5 | 5 |
| 11.5CO$_3$-HA | 11.5 | 12 |
| 15.7CO$_3$-HA | 15.7 | 15 |
| 20CO$_3$-HA | 20 | 21 |
| 24.6CO$_3$-HA | 24.6 | 25 |

TGA: thermogravimetric analysis.

**Table 4.** Silicon content (as an average of 10 area scans on EDX) and corresponding yields.

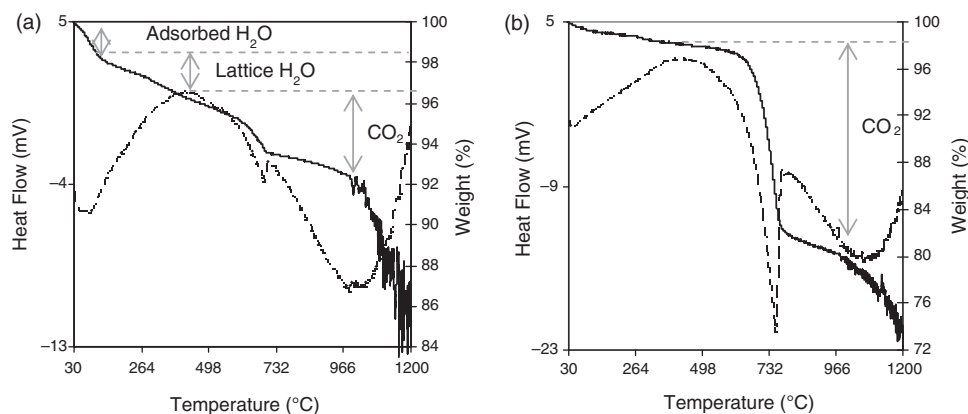| Sample ID | Expected silicon content in HA (wt%) | Silicon content in sample (wt%) | Yield (%) |
|---|---|---|---|
| 1SiHA | 1 | 0.26 | 77 |
| 2SiHA | 2 | 0.39 | 76 |
| 3SiHA | 3 | 0.56 | 75 |
| 4SiHA | 4 | 0.53 | 56 |
| 5SiHA | 5 | 0.81 | 48 |
| 6SiHA | 6 | 0.63 | 50 |
| 8SiHA | 8 | 0.93 | 41 |
| 10SiHA | 10 | 1.05 | 30 |

EDX: Energy-dispersive X-ray spectroscopy.



**Figure 4.** STA data showing DSC (dotted line) and TGA (solid line) plots for samples: (a) 7.5CO$_3$-HA, and (b) 24.6CO$_3$-HA. STA: simultaneous thermal analysis; DSC: differential scanning calorimetry; TGA: thermogravimetric analysis.

Detailed elemental quantities are given in Supplementary Data Table 2.

Figure 5 shows the variation in surface areas with increasing carbonate content (determined using TGA) for carbonate-substituted samples. There was little or no change in surface area with increase in urea content with all the surface areas falling in the range 20.8–27.5 $m^2/g$. Although the TEM images in Figure 2(a) to (c) revealed decreasing crystallite size with increase in urea in solution, it was also observed that the particles appeared to be more agglomerated and less distinct (Figure 2(c)). This might account for the slight decrease in surface area witnessed for samples 20CO$_3$-HA and 24.6CO$_3$-HA.

Figure 5 also shows the variation in surface areas with silicon content in silicate-substituted samples. It was observed that the surface area increases slightly for sample 2SiHA ($41 m^2/g$) but overall remains relatively unchanged in the range 31.1–35.4 $m^2/g$. This result suggested that the amount of silicon substituting into HA was not too different for all samples. Indeed, this was confirmed by elemental analysis shown in Table 4.

Powder X-ray diffraction data was collected for all samples in order to analyse the effect of carbonate and silicate substitution on crystallinity and phase-purity.

XRD pattern for sample 7.5CO$_3$-HA in Figure 6(a) gave a good match to line pattern for phase-pure HA (ICDD pattern 09-0432). XRD pattern in Figure 6(b) shows the on-set of formation of calcium carbonate (compared to ICDD pattern 47-1473, calcite) in sample 11.5CO$_3$-HA. With increasing carbonate content, it was seen in Figure 6(c) (for sample 15.7CO$_3$-HA) and Figure 6(d) (for sample 20CO$_3$-HA) that the peaks corresponding to calcium carbonate (calcite) increased in intensity. Peaks at 31.8° and 32.2°, corresponding to HA, became broader with increasing carbonate content, the peaks in Figure 6(e) for sample 24.6CO$_3$-HA being clearly less distinct as compared to Figure 6(a) for sample 7.5CO$_3$-HA. This was possibly due to decrease in particle size (as seen in TEM images) and crystallinity.

Figure 7 shows the XRD patterns of sample 7.5CO$_3$-HA heat treated at 730°C, 850°C and 990°C for 1 h. These temperatures were chosen from the corresponding TGA plot of the same sample. As compared to Figure 6(a) peaks corresponding to HA in Figure 7 were understandably sharper (due to crystallisation upon heating). Heat treatment at 730°C resulted in phase-pure crystalline HA (Figure 7(a)). This confirmed that the corresponding weight loss in the TGA plot shown in Figure 4(a) was not due to any thermal
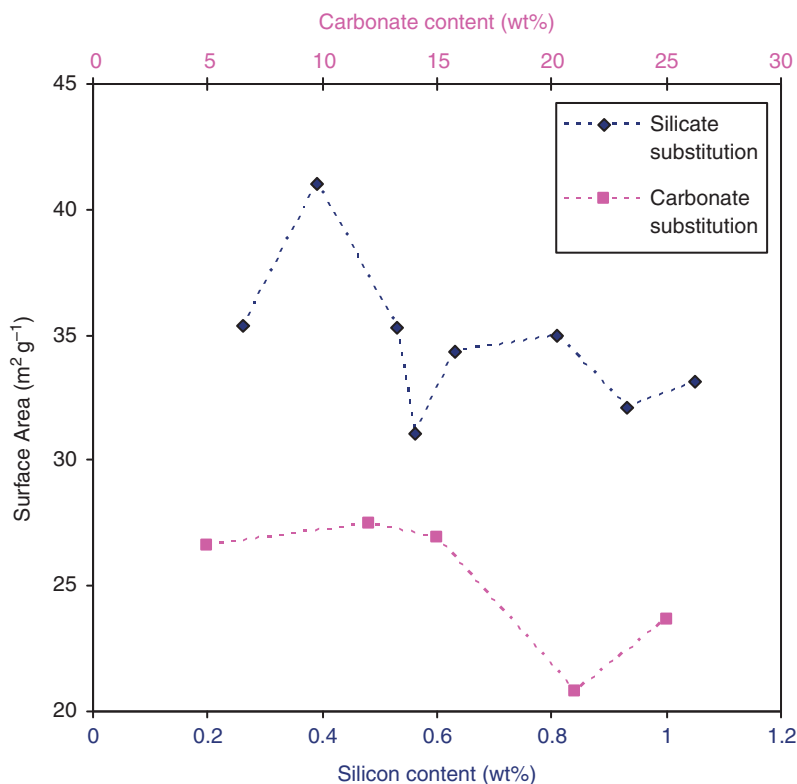


**Figure 5.** BET surface area of carbonate and silicate substituted samples as function of substitution levels.
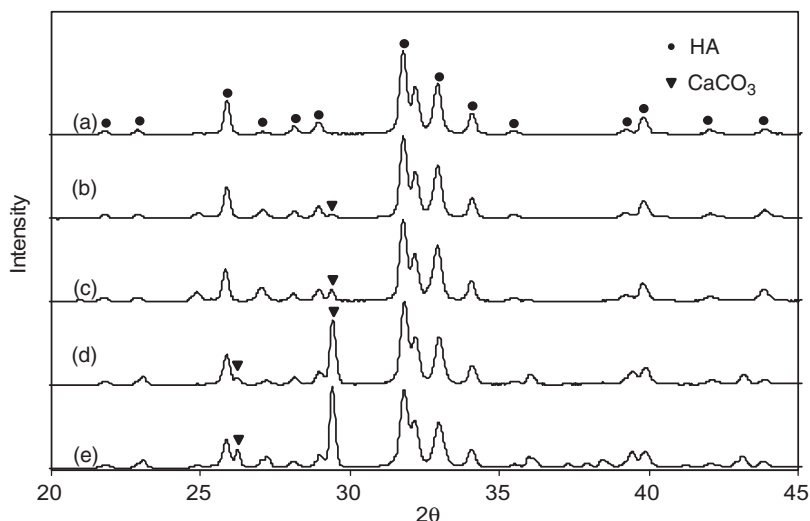
**Figure 6.** X-ray diffraction patterns of samples: (a) 7.5CO$_3$-HA; (b) 11.5CO$_3$-HA; (c) 15.7CO$_3$-HA; (d) 20CO$_3$-HA; and (e) 24.6CO$_3$-HA.
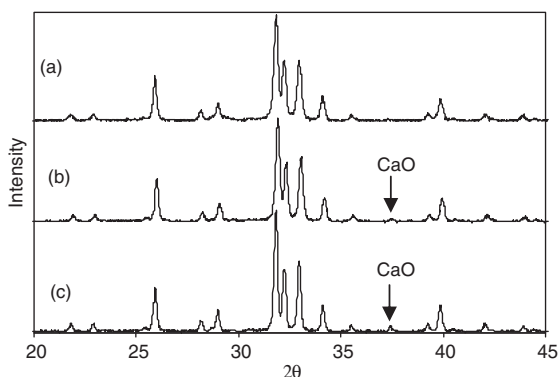


**Figure 7.** X-ray diffraction patterns of sample 7.5CO$_3$-HA heat treated at: (a) 730°C; (b) 850°C; and (c) 990°C.

decomposition and correctly represented CO$_2$ loss. However, heat treatment at 850°C and 990°C resulted in appearance of a small peak of calcium oxide (compared to ICDD pattern 37-1497). This was due to thermal decomposition of calcium deficient HA lattice for sample 7.5CO$_3$-HA.

All XRD patterns for silicate-substituted samples in Figure 8 gave a good match to JCPDS pattern 09-432, corresponding to crystalline HA. Figure 8(a) to (h) revealed no visible effect of increasing silicon content on phase-purity or crystallinity of the HA phase. This result and the decrease in percentage yield from 77% (for sample 1SiHA) to 33% (for 10SiHA) suggested that the progressive addition of the silicate precursor gave increasingly lower yields and reached a maximum substitution level under such CHFS conditions used herein. The main crystallographic planes (*hkl*) are also marked on the corresponding peaks in Figure 8.

Raman spectroscopy was carried out in order to reinforce crystallographic observations and assess phase purity. Figure 9 shows Raman spectra for all the carbonate-substituted samples. In Figure 9(a) for sample 7.5CO$_3$-HA the very weak peak at 1090 cm$^{-1}$ corresponded to asymmetric stretching ($\nu_1$) of the C–O bond in carbonate from calcium carbonate (calcite).[76] However, this was not observed in the corresponding XRD pattern, shown in Figure 6(a). This suggested that this peak might be due to asymmetric stretching ($\nu_3$) of the P–O bond in phosphate. The increase in the intensity of peak at 1090 cm$^{-1}$ in Figure 9(a) to (e) was due to an increase in calcium carbonate content, as confirmed by analogous XRD data. Peaks at 1072 and 1048 cm$^{-1}$ corresponded to asymmetric stretching ($\nu_3$) of the P–O bond in phosphate. The peak at 1072 cm$^{-1}$ may also represent symmetric stretching ($\nu_1$) of the C–O bond in carbonate.[77,78] With an increase in carbonate content it was observed that the peak at 1072 cm$^{-1}$ increased in intensity (for samples 7.5CO$_3$-HA, 11.5CO$_3$-HA and 15.7CO$_3$-HA in Figure 9(a) to (c), respectively). This peak was partially obscured by the peak at 1090 cm$^{-1}$ for samples 20CO$_3$-HA and 24.6CO$_3$-HA as shown in Figure 9(d) and (e), respectively. In Figure 9(a), peak at 961 cm$^{-1}$ corresponded to the symmetric stretching mode ($\nu_1$) of the P–O bond in phosphate, whilst peaks at 606 cm$^{-1}$, 593 cm$^{-1}$ and 581 cm$^{-1}$ corresponded to $\nu_4$ bending modes of the O–P–O linkage in phosphate. The peaks at 444 cm$^{-1}$ and 435 cm$^{-1}$ corresponded to $\nu_2$ bending modes of the O–P–O linkage in phosphate. The appearance of a weak peak at 712 cm$^{-1}$ in Figure 9(d) and (e) was possibly due to bending mode ($\nu_4$) of the O–C–O linkage in carbonate from larger amounts of calcite present in samples 20CO$_3$-HA and 24.6CO$_3$-HA.[76]
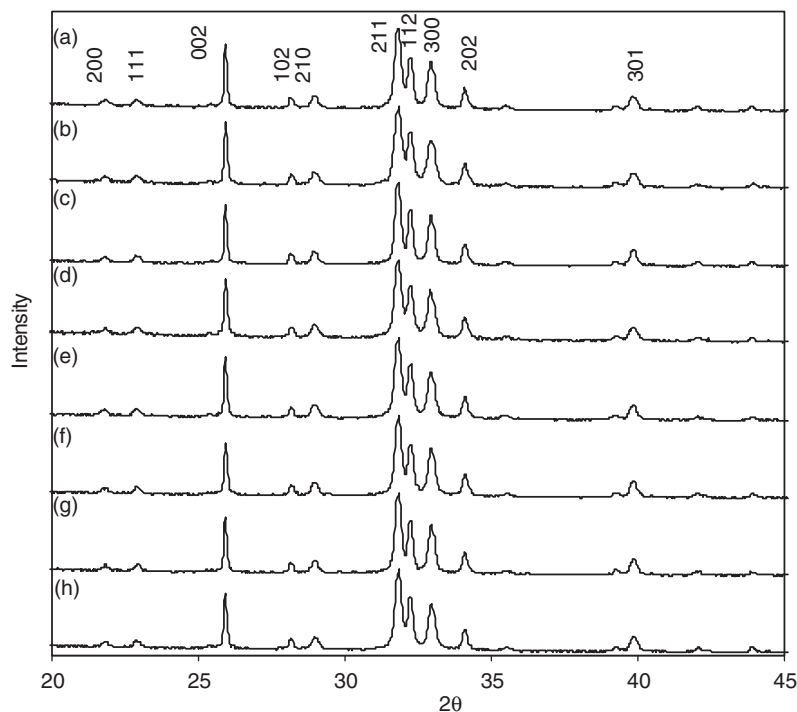
**Figure 8.** X-ray diffraction patters for samples: (a) 1SiHA; (b) 2SiHA; (c) 3SiHA; (d) 4SiHA; (e) 5SiHA; (f) 6SiHA; (g) 7SiHA; and (h) 8SiHA.
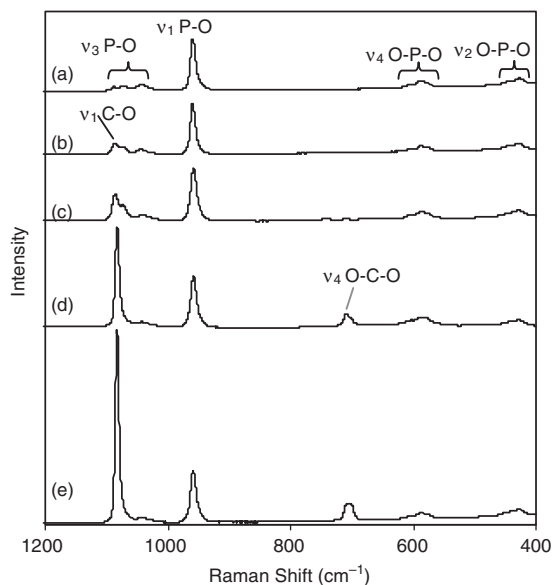


**Figure 9.** Raman spectroscopy data for the range 1200–400 cm$^{-1}$ for samples: (a) 7.5CO$_3$-HA; (b) 11.5CO$_3$-HA; (c) 15.7CO$_3$-HA; (d) 20CO$_3$-HA; and (e) 24.6CO$_3$-HA.
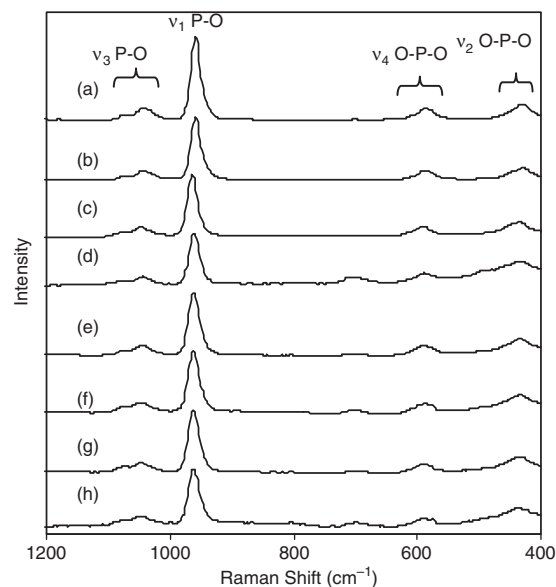


**Figure 10.** Raman spectroscopy data in the range 1200–400 cm$^{-1}$ for samples: (a) 1SiHA; (b) 2SiHA; (c) 3SiHA; (d) 4SiHA; (e) 5SiHA; (f) 6SiHA; (g) 8SiHA; and (h) 10SiHA.

Raman spectra for all silicon-substituted samples are shown in Figure 10. Figure 10(a) showing the Raman spectrum for sample 1SiHA revealed peaks at 1080 cm$^{-1}$ and 1049 cm$^{-1}$ attributed to asymmetric stretching ($v_3$) of the P–O bond in phosphate. The

peak around 960 cm$^{-1}$ corresponded to the symmetric stretching mode ($v_1$) of the P–O bond in phosphate (as in the case with carbonate-substituted samples). Peaks at 595 and 438 cm$^{-1}$ corresponded to the $v_4$ and $v_2$ bending, respectively, of the O–P–O linkage

in phosphate. No change was observed in Figure 10(a) to (h) with increasing silicon content in solution.

FTIR spectroscopy was carried out on all carbonate- and silicate-substituted samples in order to aid observations made using XRD and Raman spectroscopy. Figure 11 shows the FTIR spectra of the carbonate-substituted samples. In Figure 11(a) for sample $7.5CO_3$-HA, peaks at 3570 and 633 $cm^{-1}$ corresponded to stretching mode ($v_s$) and liberational mode ($v_L$) of the hydroxyl group in a HA lattice. The bands in the range 1590–1300 $cm^{-1}$ corresponded to asymmetric stretching ($v_3$) of the C–O bond of carbonate in both A- and B-type carbonate substitutions in HA. However given the fact that CHFS is a wet chemical method, B-type carbonate substitution was expected (where carbonate ions are substituted for phosphate ions in the HA lattice). This is also supported by the observation that the peak at 3570 $cm^{-1}$ did not diminish with an increase in urea concentration in the reagent solution suggesting that carbonate substitution for hydroxyl groups in the HA lattice does not take place. With an increase in urea concentration there was an increase in the intensity of the bands in the range 1590–1300 $cm^{-1}$, corresponding to carbonate asymmetric stretching (Figure 11(a) and (b) representing samples $7.5CO_3$-HA and $11.5CO_3$-HA, respectively]. This may be due to increased carbonate substitution into the HA lattice and/or appearance of calcite. The band 1090–1030 $cm^{-1}$ corresponded to asymmetric stretching modes ($v_3$) of the P–O bond in

phosphate. Peak at 961 $cm^{-1}$ corresponded to the symmetric stretching mode ($v_1$) of the P–O bonds of phosphate. In Figure 11(a) the peak at 876 $cm^{-1}$ corresponded to the bending mode ($v_2$) of the O–C–O linkage in carbonate. This peak showed a marked increase in intensity with an increase in amount of urea concentration in solution as witnessed in Figures 11(b) to (e). Peaks at 603 $cm^{-1}$, 568 $cm^{-1}$ and 472 $cm^{-1}$ in Figure 11(a) corresponded to bending modes of O–P–O linkages in phosphate. From the FTIR data it was observed that the carbonate peaks (1590–1300 $cm^{-1}$ and 876 $cm^{-1}$) reached their maximum intensity for $11.5CO_3$-HA in Figure 11(b). Any further increase in amount of urea concentration in reagent solutions contributed to more formation of calcium carbonate as seen in analogous XRD and Raman data. In Figure 11(d), for sample $20CO_3$-HA, a peak appeared at 1793 $cm^{-1}$ which has been reported to be due to presence of calcite.[79] Gunasekaran et al.[76] reported a peak at 1798 $cm^{-1}$ for calcite and attributed it to a combination of asymmetric stretching ($v_1$) and bending ($v_4$) of bonds related to carbonate. Also, in the same spectrum, a shoulder appeared at 865 $cm^{-1}$ which resolved into a peak for sample $24.6CO_3$-HA in Figure 11(e). This peak was attributed to the bending mode ($v_2$) of the O–C–O linkage in carbonate from calcite.[76] Peak at 713 $cm^{-1}$ for samples $20CO_3$-HA and $24.6CO_3$-HA in Figure 11(d) and (e) corresponded to bending mode ($v_4$) of the O–C–O linkage in carbonate from calcite.
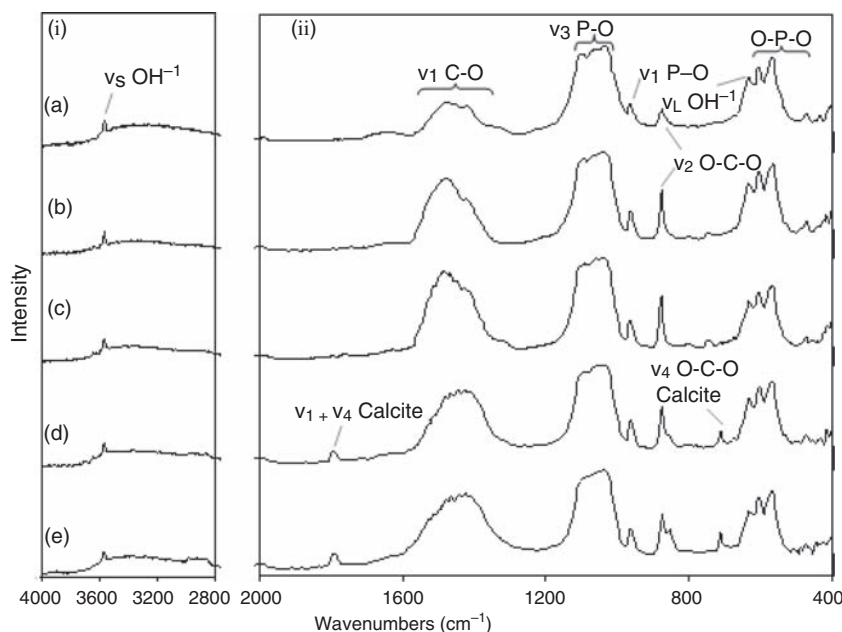


**Figure 11.** FTIR data for ranges (i) 3800–2800 $cm^{-1}$ and (ii) 2000–400 $cm^{-1}$ for samples: (a) $7.5CO_3$-HA; (b) $11.5CO_3$-HA; (c) $15.7CO_3$-HA; (d) $20CO_3$-HA; and (e) $24.6CO_3$-HA.
FTIR: Fourier transform infrared.

The FTIR spectrum for sample 1SiHA in Figure 12(a) revealed peaks similar to those observed for carbonate-substituted samples. However, the weak band in the range 1565–1380 cm$^{-1}$ (corresponding to asymmetric stretching ($v_3$) of the C–O bond of carbonate in both A- and B-type carbonate substitutions in HA) was understandably much lower in intensity as compared to the intensity of the similar band seen in the FTIR spectrum of carbonate substitutes samples in Figure 11. The weak peak centred at ~872 cm$^{-1}$ due to the bending mode ($v_2$) of the O–C–O linkage in a small amount of carbonate which is present, was lower in intensity as compared to the similar peak observed at 876 cm$^{-1}$ in Figure 11(a) (due to higher amount of carbonate ions present in carbonate-substituted samples). A notable difference from the FTIR spectrum seen in Figure 11 was that the OH$^{-1}$ stretching peak at 3571 cm$^{-1}$ decreased in intensity with increasing silicon substitution (Figure 12(a) to (h)). This confirmed that silicon was being substituted in the HA lattice in the form of silicate, SiO$_4^{4-}$ substituting phosphate, PO$_4^{3-}$. In order to maintain the charge balance, OH$^{-1}$ is lost, causing a decrease in intensity of the OH$^{-1}$ peak at 3571 cm$^{-1}$. Furthermore, it was noticed that increasing silicon content increased the intensity of the carbonate band in the range 1560–1380 cm$^{-1}$. This was possibly due to incorporation of CO$_3^{2-}$ as a result of charge compensation as shown in the following equation.

$$2PO_4^{3-} \leftrightarrow SiO_4^{4-} + CO_3^{2-} \tag{5}$$

As we have reported earlier, the presence of carbonate peaks was unsurprising, as deionised water used in preparation of solutions and synthesis in the CHFS reactor was not degassed prior to use and may contain dissolved carbonate.[68]

$^{29}$Si MAS-NMR result for sample 5SiHA is shown in Supplementary Data Figure 2. A range of environments were seen for silicon (−72.5, −91.1 and −99.2 ppm). The most intense peak at −72.5 comes from the silicate, Si(O$^-$)$_4$ environment (Q$^0$) which corresponded to SiO$_4^{4-}$ substituting PO$_4^{3-}$ in the HA lattice wherein the silicon is not bonded to any other silicon. The peaks at −91.1 and −99.2 are possibly due to the Q$^2$ [Si(OSi)$_2$(O$^-$)$_2$] and Q$^3$ [Si(OSi)$_3$O$^-$] environments.[80,81] Gasquères et al.[82] achieved 4.6 wt% Si-HA using a precipitation method; however, they reported that only a small fraction is incorporated into HA in the form of Q$^0$ (SiO$_4^{4-}$) and the remaining silicate units were located outside the HA structure and corresponded to silica-gel units.
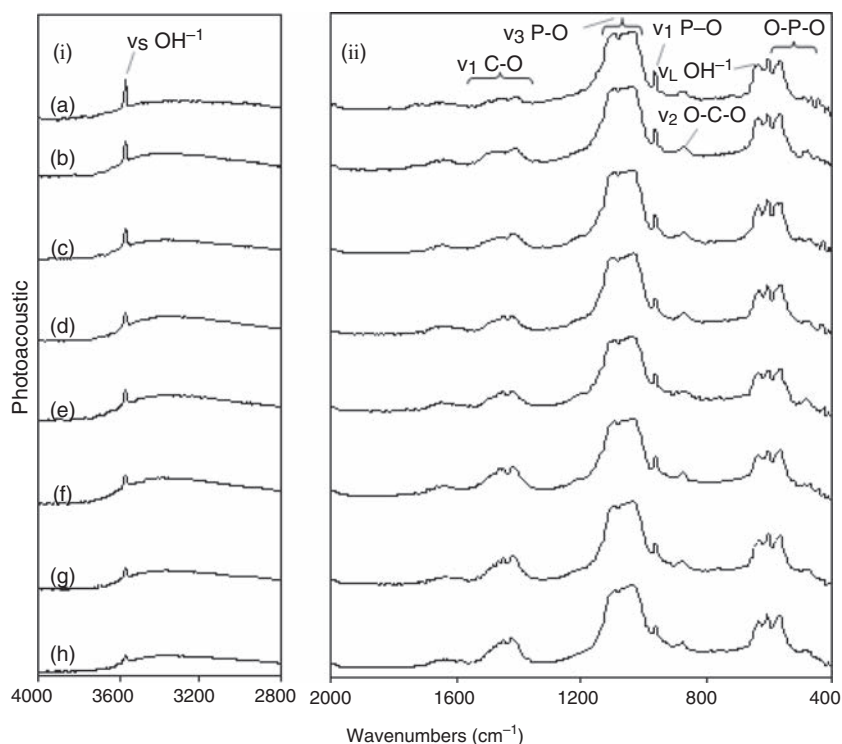


**Figure 12.** FTIR spectroscopy data for samples (a) 1SiHa; (b) 2SiHa; (c) 3SiHa; (d) 4SiHa; (e) 5SiHa; (f) 6SiHa; (g) 8SiHa; (h) 10SiHa. FTIR: Fourier transform infrared.

## Conclusions

In this work, the capability of the CHFS to synthesise substituted HA nanoparticles with tailorable properties in a rapid single step manner was highlighted. Phase pure, crystalline and nano-sized carbonate-substituted HA with ~5 wt% substituted carbonate content (sample 7.5CO$_3$-HA) was synthesised using the CHFS system using urea as a carbonate source. It was observed that a further increase in urea concentration in solution resulted in biphasic mixtures of carbonate-substituted HA and calcium carbonate (calcite). Increase in urea concentration in solution also decreased the particle size of HA. Sample 7.5CO$_3$-HA was found to be calcium deficient with a Ca:P molar ratio of 1.45 (±0.04) which is akin to biological apatite, a calcium deficient carbonate-substituted HA.

Phase-pure crystalline and nano-sized silicate-substituted HA was also synthesised using the CHFS system with silicon acetate as a silicate ion source. The silicon content in samples increased with increasing silicon acetate concentration in the solution and a maximum of ~1.1 wt% substituted silicon content was obtained. However, it is hypothesised that a substitution threshold of ~1.1 wt% for this method exists for silicate-substituted HA made in the CHFS system (using silicon acetate as a silicate ion source).

## References

1. Porter AE, Best SM and Bonfield W. Ultrastructural comparison of hydroxyapatite and silicon-substituted hydroxyapatite for biomedical applications. *J Biomed Mater Res Part A* 2004; 68A: 133–141.
2. Barralet JE, Fleming GJP, Campion C, et al. Formation of translucent hydroxyapatite ceramics by sintering in carbon dioxide atmospheres. *J Mater Sci* 2003; 38: 3979–3993.
3. Wopenka B and Pasteris JD. A mineralogical perspective on the apatite in bone. *Mater Sci Eng C-Biomimetic Supramol Syst* 2005; 25: 131–143.
4. Webster TJ, Massa-Schlueter EA, Smith JL, et al. Osteoblast response to hydroxyapatite doped with divalent and trivalent cations. *Biomaterials* 2004; 25: 2111–2121.
5. LeGeros RZ. Properties of osteoconductive biomaterials: calcium phosphates. *Clin Orthopaed Relat Res* 2002; 395: 81–98.
6. Leventouri T. Synthetic and biological hydroxyapatites: crystal structure questions. *Biomaterials* 2006; 27: 3339–3342.
7. Bansal S, Chauhan V, Sharma S, et al. Evalutation of hydroxyapatite and beta-tricalcium phosphate mixed with bone marrow aspirate as a bone graft substitute for posterolateral spinal fusion. *Ind J Orthoped* 2009; 43: 234–239.
8. Haque S, Rehman I and Darr JA. Synthesis and characterization of grafted nanohydroxyapatites using functionalized surface agents. *Langmuir* 2007; 23: 6671–6676.
9. Moshaverinia A, Ansari S, Moshaverinia M, et al. Effects of incorporation of hydroxyapatite and fluoroapatite nanobioceramics into conventional glass ionomer cements (GIC). *Acta Biomater* 2008; 4: 432–440.
10. Moshaverinia A, Ansari S, Movasaghi Z, et al. Modification of conventional glass-ionomer cements with N-vinylpyrrolidone containing polyacids, nano-hydroxy and fluoroapatite to improve mechanical properties. *Dental Mater* 2008; 24: 1381–1390.
11. Kenny SM and Buggy M. Bone cements and fillers: a review. *J Mater Sci-Mater Med* 2003; 14: 923–938.
12. Baramki HG, Steffen T, Lander P, et al. The efficacy of interconnected porous HA in achieving posterolateral lumbar fusion in sheep. *Spine* 2000; 25: 1053–1060.
13. Darr JA, Guo ZX, Raman V, et al. Metal organic chemical vapour deposition (MOCVD) of bone mineral like carbonated hydroxyapatite coatings. *Chem Commun* 2004; 696–697.
14. Thian ES, Huang J, Vickers ME, et al. Silicon-substituted hydroxyapatite (SiHA): a novel calcium phosphate coating for biomedical applications. *J Mater Sci* 2006; 41: 709–717.
15. Barralet J, Best S and Bonfield W. Carbonate substitution in precipitated hydroxyapatite: an investigation into the effects of reaction temperature and bicarbonate ion concentration. *J Biomed Mater Res* 1998; 41: 79–86.
16. Barralet J, Akao M, Aoki H, et al. Dissolution of dense carbonate apatite subcutaneously implanted in Wistar rats. *J Biomed Mater Res* 2000; 49: 176–182.
17. Ito A, Maekawa K, Tsutsumi S, et al. Solubility product of OH-carbonated hydroxyapatite. *J Biomed Mater Res* 1997; 36: 522–528.
18. Murugan R and Ramakrishna S. Production of ultra-fine bioresorbable carbonated hydroxyapatite. *Acta Biomater* 2006; 2: 201–206.
19. Porter A, Patel N, Brooks R, et al. Effect of carbonate substitution on the ultrastructural characteristics of hydroxyapatite implants. *J Mater Sci-Mater Med* 2005; 16: 899–907.
20. Kannan S, Vieira SI, Olhero SM, et al. Synthesis, mechanical and biological characterization of ionic doped carbonated hydroxyapatite/β-tricalcium phosphate mixtures. *Acta Biomater* 2011; 7: 1835–1843.

21. Li B, Liao X, Zheng L, et al. Preparation and cellular response of porous A-type carbonated hydroxyapatite nanoceramics. *Mater Sci Eng C* 2012; 32: 929–936.

22. Elliott JC. *Structure and chemistry of the apatites and the other calcium orthophosphates*. Amsterdam: Elsevier Science, 1994.

23. Gibson IR and Bonfield W. Novel synthesis and characterization of an AB-type carbonate-substituted hydroxyapatite. *J Biomed Mater Res* 2002; 59: 697–708.

24. Kuhl G and Nebergall WH. Hydrogenphosphat- und Carbonatapatite. *Zeitschrift für anorganische und allgemeine Chemie* 1963; 324: 313–320.

25. Nelson DGA and Featherstone JDB. Preparation, analysis, and characterization of carbonated apatites. *Calcif Tissue Int* 1982; 34: S69–S81.

26. Doi Y, Moriwaki Y, Aoba T, et al. Carbonate apatites from aqueous and non-aqueous media studied by electron-spin-resonance, IR, and X-ray-diffraction - Effect of $NH_4^+$ ions on crystallographic parameters. *J Dent Res* 1982; 61: 429–434.

27. Vignoles M, Bonel G and Young RA. Occurrence of nitrogenous species in precipitated B-type carbonated hydroxyapatites. *Calcif Tissue Int* 1987; 40: 64–70.

28. Okada K, Temuujin J, Kameshima Y, et al. Simultaneous uptake of ammonium and phosphate ions by composites of gamma-alumina/potassium aluminosilicate gel. *Mater Res Bull* 2003; 38: 749–756.

29. Mizutani Y, Hattori M, Okuyama M, et al. Carbonate-containing hydroxyapatite derived from calcium tripolyphosphate gel with urea. *J Mater Sci-Mater Med* 2005; 16: 709–712.

30. Han Y, Xu KW, Montay G, et al. Evaluation of nanostructured carbonated hydroxyapatite coatings formed by a hybrid process of plasma spraying and hydrothermal synthesis. *J Biomed Mater Res* 2002; 60: 511–516.

31. Redey SA, Razzouk S, Rey C, et al. Osteoclast adhesion and activity synthetic hydroxyapatite, carbonated hydroxyapatite, and natural calcium carbonate: Relationship to surface energies. *J Biomed Mater Res* 1999; 45: 140–147.

32. Vuola J, Goransson H, Bohling T, et al. Bone marrow induced osteogenesis in hydroxyapatite and calcium carbonate implants. *Biomaterials* 1996; 17: 1761–1766.

33. Liu Y, Jiang T, Zhou Y, et al. Evaluation of the attachment, proliferation, and differentiation of osteoblast on a calcium carbonate coating on titanium surface. *Mater Sci Eng C* 2011; 31: 1055–1061.

34. Vuola J, Taurio R, Goransson H, et al. Compressive strength of calcium carbonate and hydroxyapatite implants after bone-marrow-induced osteogenesis. *Biomaterials* 1998; 19: 223.

35. Corrente G, Abundo R, Cardaropoli G, et al. Supracrestal bone regeneration around dental implants using a calcium carbonate and a fibrin-fibronectin sealing system: clinical and histologic evidence. *Int J Periodont Restorat Dent* 1997; 17: 171–177.

36. Green D, Walsh D, Yang XB, et al. Stimulation of human bone marrow stromal cells using growth factor encapsulated calcium carbonate porous microspheres. *J Mater Chem* 2004; 14: 2206–2212.

37. Thachepan S, Li M, Davis SA, et al. Additive-mediated crystallization of complex calcium carbonate superstructures in reverse microemulsions. *Chem Mater* 2006; 18: 3557–3561.

38. Hench LL. Bioceramics - from concept to clinic. *J Am Ceram Soc* 1991; 74: 1487–1510.

39. Porter AE. Nanoscale characterization of the interface between bone and hydroxyapatite implants and the effect of silicon on bone apposition. *Micron* 2006; 37: 681–688.

40. Carlisle EM. Silicon. A possible factor in bone calcification. *Science* 1970; 167: 279–280.

41. Carlisle EM. The nutritional essentiality of silicon. *Nutrit Rev* 1982; 40: 193–198.

42. Thian ES, Huang J, Best SM, et al. The response of osteoblasts to nanocrystalline silicon-substituted hydroxyapatite thin films. *Biomaterials* 2006; 27: 2692–2698.

43. Porter AE, Patel N, Skepper JN, et al. Comparison of in vivo dissolution processes in hydroxyapatite and silicon-substituted hydroxyapatite bioceramics. *Biomaterials* 2003; 24: 4609–4620.

44. Botelho CM, Brooks RA, Best SM, et al. Human osteoblast response to silicon-substituted hydroxyapatite. *J Biomed Mater Res* 2006; 79A: 723–730.

45. Patel N, Best SM, Bonfield W, et al. A comparative study on the in vivo behavior of hydroxyapatite and silicon substituted hydroxyapatite granules. *J Mater Sci-Mater Med* 2002; 13: 1199–1206.

46. Kim SR, Lee JH, Kim YT, et al. Synthesis of Si, Mg substituted hydroxyapatites and their sintering behaviors. *Biomaterials* 2003; 24: 1389–1398.

47. Gibson IR, Best SM and Bonfield W. Chemical characterization of silicon-substituted hydroxyapatite. *J Biomed Mater Res* 1999; 44: 422–428.

48. Hing KA, Revell PA, Smith N, et al. Effect of silicon level on rate, quality and progression of bone healing within silicate-substituted porous hydroxyapatite scaffolds. *Biomaterials* 2006; 27: 5014–5026.

49. Tang XL, Xiao XF and Liu RF. Structural characterization of silicon-substituted hydroxyapatite synthesized by a hydrothermal method. *Mater Lett* 2005; 59: 3841–3846.

50. Leventouri T, Bunaciu CE and Perdikatsis V. Neutron powder diffraction studies of silicon-substituted hydroxyapatite. *Biomaterials* 2003; 24: 4205.

51. Thian ES, Huang J, Best SM, et al. Novel silicon-doped hydroxyapatite (Si-HA) for biomedical coatings: an in vitro study using acellular simulated body fluid. *J Biomed Mater Res Part B-Appl Biomater* 2006; 76B: 326–333.

52. Thian ES, Huang J, Best SM, et al. Silicon-substituted hydroxyapatite: the next generation of bioactive coatings. *Mater Sci Eng C-Biomimet Supramol Syst* 2007; 27: 251–256.

53. Gibson IR, Best SM and Bonfield W. Effect of silicon substitution on the sintering and microstructure of hydroxyapatite. *J Am Ceram Soc* 2002; 85: 2771–2777.

54. Phillips MJ, Darr JA, Luklinska ZB, et al. Synthesis and characterization of nano-biomaterials with potential

osteological applications. *J Mater Sci-Mater Med* 2003; 14: 875–882.

55. Norton J, Malik KR, Darr JA, et al. Recent developments in processing and surface modification of hydroxyapatite. *Adv Appl Ceram* 2006; 105: 113–139.

56. Gong K, Braden M, Patel MP, et al. Controlled release of chlorhexidine diacetate from a porous methacrylate system: supercritical fluid assisted foaming and impregnation. *J Pharmaceut Sci* 2007; 96: 2048–2056.

57. Gribov EN, Parkhomchuk EV, Krivobokov IM, et al. Supercritical $CO_2$ assisted synthesis of highly selective nafion-zeolite nanocomposite membranes for direct methanol fuel cells. *J Membr Sci* 2007; 297: 1–4.

58. Darr JA, Poliakoff MA, Li WS, et al. Hexafluoropentanedionatosilver(I) complexes stabilised by multidentate N-donor ligands: crystal structure of a charge-separated salt species soluble in supercritical carbon dioxide. *J Chem Soc-Dalton Trans* 1997; 17: 2869–2874.

59. Ma J, Bilotti E, Peijs T, et al. Preparation of polypropylene/sepiolite nanocomposites using supercritical $CO_2$ assisted mixing. *Eur Polym J* 2007; 43: 4931–4939.

60. Kafizas A, Kellici S, Darr JA, et al. Titanium dioxide and composite metal/metal oxide titania thin films on glass: a comparative study of photocatalytic activity. *J Photochem Photobiol A-Chem* 2009; 204: 183–190.

61. Middelkoop V, Boldrin P, Peel M, et al. Imaging the inside of a continuous nanoceramic synthesizer under supercritical water conditions using high-energy synchrotron X-radiation. *Chem Mater* 2009; 21: 2430–2435.

62. Weng XL, Perston B, Wang XZ, et al. Synthesis and characterization of doped nano-sized ceria-zirconia solid solutions. *Appl Catal B-Environ* 2009; 90: 405–415.

63. Thompson K, Goodall J, Kellici S, et al. Screening tests for the evaluation of nanoparticle titania photocatalysts. *J Chem Technol Biotechnol* 2009; 84: 1717–1725.

64. Zhang Z, Goodall JBM, Brown S, et al. Continuous hydrothermal synthesis of extensive 2D sodium titanate (Na2Ti3O7) nano-sheets. *Dalton Trans* 2010; 39: 711–714.

65. Kellici S, Gong K, Lin T, et al. High throughput continuous hydrothermal (HiTCH) flow synthesis of Zn-Ce oxides: unprecedented solubility of Zn in the nanoparticle fluorite lattice. *Philos Transact A Math Phys Eng Sci* 2010; 368: 4331–4349.

66. Darr JA, Weng X, Brett D, et al. Highly conductive low nickel content nano-composite dense cermets from nano-powders made via a continuous hydrothermal synthesis route. *Solid State Ionics* 2010; 181: 827–834.

67. Lin T, Kellici S, Gong K, et al. The rapid automated materials synthesis instrument (RAMSI): exploring the composition and heat-treatment of nano-precursors towards low temperature red phosphors. *J Comb Chem* 2010; 12: 383–392.

68. Chaudhry AA, Haque S, Kellici S, et al. Instant nano-hydroxyapatite: a continuous and rapid hydrothermal synthesis. *Chem Commun* 2006; 2286–2288.

69. Chaudhry AA, Goodall J, Vickers M, et al. Synthesis and characterisation of magnesium substituted calcium phosphate bioceramic nanoparticles made via continuous hydrothermal flow synthesis. *J Mater Chem* 2008; 18: 5900–5908.

70. Chaudhry AA, Yan H, Viola G, et al. Phase stability and rapid consolidation of hydroxyapatite-zirconia nanocoprecipitates made using continuous hydrothermal flow synthesis. *J Biomater Appl* 2012; 27: 79–90.

71. Chaudhry AA, Yan H, Gong K, et al. High-strength nanograined and translucent hydroxyapatite monoliths via continuous hydrothermal synthesis and optimized spark plasma sintering. *Acta Biomater* 2011; 7: 791–799.

72. Boldrin P, Hebb AK, Chaudhry AA, et al. Direct synthesis of nanosized $NiCo_2O_4$ spinel and related compounds via continuous hydrothermal synthesis. *Ind Eng Chem Res* 2007; 46: 4830–4838.

73. Weng XL, Boldrin P, Abrahams I, et al. Direct syntheses of mixed ion and electronic conductors $La_4Ni_3O_{10}$ and $3Ni_2O_7$ from nanosized coprecipitates. *Chem Mater* 2007; 19: 4382–4384.

74. Weng XL, Cockcroft JK, Hyett G, et al. High-throughput continuous hydrothermal synthesis of an entire nano-ceramic phase diagram. *J Comb Chem* 2009; 11: 829–834.

75. Wang C, Zhao J, Zhao X, et al. Synthesis of nanosized calcium carbonate (aragonite) via a polyacrylamide inducing process. *Powder Technol* 2006; 163: 134–138.

76. Gunasekaran S, Anbalagan G and Pandi S. Raman and infrared spectra of carbonates of calcite structure. *J Raman Spectrosc* 2006; 37: 892–899.

77. Penel G, Leroy G, Rey C, et al. MicroRaman spectral study of the $PO_4$ and $CO_3$ vibrational modes in synthetic and biological apatites. *Calcif Tissue Int* 1998; 63: 475–481.

78. Awonusi A, Morris M and Tecklenburg M. Carbonate assignment and calibration in the Raman spectrum of apatite. *Calcif Tissue Int* 2007; 81: 46–52.

79. Jackson KDO. A guide to identifying common inorganic fillers and activators using vibrational spectroscopy. *Internet J Vibr Spectr* 1998; 2–3.

80. Diaz A, Lopez T, Manjarrez J, et al. Growth of hydroxyapatite in a biocompatible mesoporous ordered silica. *Acta Biomater* 2006; 2: 173–179.

81. Fujii E, Kawabata K, Ando K, et al. Synthesis and structural characterization of silica-hybridized hydroxyapatite with gas adsorption capability. *J Ceram Soc Jpn* 2006; 114: 769–773.

82. Gasqueres G, Bonhomme C, Maquet J, et al. Revisiting silicate substituted hydroxyapatite by solid-state NMR. *Magn Reson Chem* 2008; 46: 342–346.